

PREPARED FOR SUBMISSION TO JINST

DECEMBER 27TH, 2021

A Novel Nuclear Emulsion Detector for Measurement of Quantum States of Ultracold Neutrons in the Earth's Gravitational Field

**Naoto Muto¹ Hartmut Abele² Tomoko Ariga³ Joachim Bosina^{2,4} Masahiro Hino⁵
Katsuya Hirota^{1,6} Go Ichikawa^{6,7} Tobias Jenke⁴ Hiroaki Kawahara¹ Shinsuke Kawasaki⁶
Masaaki Kitaguchi^{1,8} Jakob Micko^{2,4} Kenji Mishima^{6,7} Naotaka Naganawa^{1,9}
Mitsuhiro Nakamura^{1,8,9} Stéphanie Roccia⁴ Osamu Sato^{1,9} René I. P. Sedmik²
Yoshichika Seki¹⁰ Hirohiko M. Shimizu^{1,6} Satomi Tada¹ Atsuhiro Umemoto^{1,11}**

¹*Department of Physics, Nagoya University,*

*Furo-cho, Chikusa-ku, Nagoya, 464-8601, Japan; muto@flab.phys.nagoya-u.ac.jp,
hirota@phi.phys.nagoya-u.ac.jp, kawahara@flab.phys.nagoya-u.ac.jp, kitaguchi@phi.phys.nagoya-u.ac.jp,
naganawa@flab.phys.nagoya-u.ac.jp, nakamura@flab.phys.nagoya-u.ac.jp, sato@flab.phys.nagoya-u.ac.jp,
shimizu@phi.phys.nagoya-u.ac.jp, tada@flab.phys.nagoya-u.ac.jp*

²*Atominstytut, Technische Universität Wien,*

*Stadionallee 2, 1020 Vienna, Austria; hartmut.abele@tuwien.ac.at, joachim.bosina@tuwien.ac.at,
rene.sedmik@tuwien.ac.at*

³*Kyushu University,*

744 Motooka Nishi-ku, Fukuoka, 819-0395, Japan; tomoko.ariga@cern.ch

⁴*Institut Laue-Langevin,*

*71 avenue des Martyrs CS 20156, 38042 GRENOBLE Cedex 9, France; jenke@ill.fr, micko@ill.fr,
roccia@ill.fr*

⁵*Institute for Integrated Radiation and Nuclear Science, Kyoto University,*

Kumatori, Osaka, 590-0494, Japan; hino.masahiro.2x@kyoto-u.ac.jp

⁶*High Energy Accelerator Research Organization (KEK),*

Tsukuba, Ibaraki, 305-0801, Japan; go.ichikawa@kek.jp, shinsuke.kawasaki@kek.jp, kenji.mishima@kek.jp

⁷*Japan Proton Accelerator Research Complex (J-PARC) Center,*

Tokai, Ibaraki, 319-1195, Japan

⁸*Kobayashi-Maskawa Institute for Origin of Particles and the Universe (KMI), Nagoya University,*

Furo-cho, Chikusa-ku, Nagoya, 464-8601, Japan

⁹*Institute of Materials and Systems for Sustainability, Nagoya University,*

Furo-cho, Chikusa-ku, Nagoya, 464-8601, Japan

¹⁰*Center for Physics and Mathematics, Osaka Electro-Communication University,*

Neyagawa, Osaka 572-8530, Japan; seki@osakac.ac.jp

¹¹*Division of Physics, University of Tsukuba,*

Tennodai, Tsukuba 305-8571, Japan; umemoto.atsuhiro.gu@u.tsukuba.ac.jp

E-mail: muto@flab.phys.nagoya-u.ac.jp

ABSTRACT: Hypothetical short-range interactions could be detected by measuring the wavefunctions of gravitationally bound ultracold neutrons on a mirror in the Earth's gravitational field. Searches for them with higher sensitivity require detectors with higher spatial resolution. We developed and have been improving an ultracold neutron detector with a high spatial resolution, which consists of a Si substrate, a thin converter layer including $^{10}\text{B}_4\text{C}$, and a layer of fine-grained nuclear emulsion. Its resolution was estimated to be less than 100 nm by fitting tracks of either ^7Li nuclei or α -particles, which were created when neutrons interacted with the $^{10}\text{B}_4\text{C}$ layer. For actual measurements of the spatial distributions, the following two improvements were made. The first improvement was to establish a method to align microscopic images with high accuracy within a wide region of $65\text{ mm} \times 0.2\text{ mm}$. We created reference marks of $1\text{ }\mu\text{m}$ and $5\text{ }\mu\text{m}$ diameter with an interval of $50\text{ }\mu\text{m}$ and $500\text{ }\mu\text{m}$, respectively, on the Si substrate by electron beam lithography and realized a position accuracy of less than 30 nm. The second improvement was to build a holder for the detector that could maintain the atmospheric pressure around the nuclear emulsion to utilize it under vacuum during exposure to ultracold neutrons.

The intrinsic resolution of the improved detector was estimated to be better than $0.56(8)\text{ }\mu\text{m}$ by evaluating the blur of a transmission image of a gadolinium grating taken by cold neutrons. The evaluation included the precision of the gadolinium grating. A test exposure to ultracold neutrons was conducted to obtain the spatial distribution of ultracold neutrons in the Earth's gravitational field. Although the test was successful, a blurring of $6.9\text{ }\mu\text{m}$ was found in the measurements, compared with a theoretical curve. As the reason for the blurring, we identified the increased refraction of neutrons due to the roughness of the upstream surface of the substrate. By polishing the surface, it may be possible to analyze the distribution with a resolution of less than 100 nm in future experiments.

KEYWORDS: Gravity experiment, Ultracold neutron, Nuclear emulsion

Contents

1	Introduction	1
2	Improvements of the detector	4
3	Measurement of the resolution using a gadolinium grating	7
4	Measurement of the spatial distribution of quantized UCNs	14
5	Conclusion	22

1 Introduction

Hypothetical fields manifesting as dark energy or dark matter may also lead to interactions causing effective deviations from Newtonian gravity at short distances. In recent years, various experiments have been searching for such interactions [1]. Some of them have been searching hypothetical fields by measuring the spatial distributions of quantized states of ultracold neutrons (UCNs) bound by the Earth's gravitational potential on mirrors and comparing those distributions to theoretical curves including only Newtonian gravity [2–4]. Those distributions have characteristic structures in the scale of ten micrometers, and therefore they require detectors with a high spatial resolution of not more than a few micrometers. The sensitivity of those experiments depends on the spatial resolution of the detectors and the experimental setup including mirrors. The *qBOUNCE* collaboration [3] developed and utilized a CR39 detector with a ^{10}B converter layer [5] with a resolution of $1.5\ \mu\text{m}$. In another experiment [4], a Ni-coated cylindrical glass rod was used to expand the image and measure the distribution with a resolution of $0.7\ \mu\text{m}$. To further increase the sensitivity, a detector with a higher spatial resolution is necessary. We have developed such a detector based on a fine-grained nuclear emulsion.

Nuclear emulsions consist of silver halide crystals dispersed in gelatin. Particles passing through the emulsion leave a linear series of silver grains (a track) that can be detected optically. The high spatial resolution of these tracks has led to important results in nuclear and particle physics, such as the discovery of π mesons [6], studies on double hypernuclei [7–9], and the first detection of tau neutrino interactions [10]. Recently, a fine-grained nuclear emulsion was developed for use in experiments searching for dark matter [11]. With a crystal size of $40\ \text{nm}$ and a density of 13 crystals per μm , our emulsion detectors are 6 times denser and have 5 times smaller crystals than a normal emulsion, thereby improving the spatial resolution. In addition, no track is formed by minimum ionizing particles or electrons produced by γ -rays occurring as background in neutron experiments because silver halide crystals have small sizes and have not been sensitized.

Emulsion detectors can be sensitive to cold neutrons or UCNs when using a $^{10}\text{B}_4\text{C}$ conversion layer sputtered onto a Si substrate, followed by NiC, and C layers [12]. The emulsion is applied above

the C top layer (Figure 1). NiC and C act as stabilizers for $^{10}\text{B}_4\text{C}$ and the emulsion, respectively. The thickness of $^{10}\text{B}_4\text{C}$, NiC, and C are 200 nm, 60 nm, and 20 nm, respectively. When neutrons interact with the $^{10}\text{B}_4\text{C}$ layer, ^7Li nuclei and α -particles are emitted back-to-back by neutron capture reactions and either of them passes through the emulsion layer. The detection efficiency is estimated to be 40 % for neutron velocities around 10 m/s. The emulsion is capable of recording tracks of ^7Li nuclei with a range of 2.7(4) μm or α -particles with a range of 5.2(4) μm in the emulsion, calculated by SRIM-2013 based on the composition of the recent fine-grained nuclear emulsion. Tracks from the absorption points of neutrons were observed under an optical microscope with an epi-illumination system [13]. The wavelength of the illumination was 455 nm, and the microscope was equipped with a CMOS image sensor. We used an oil immersion lens with magnification 100 \times , and a numerical aperture of 1.45. As a feature of the detector, both real and mirror images of the tracks are obtained because the surface of the C layer in the substrate functions as an optical mirror (Figure 2).

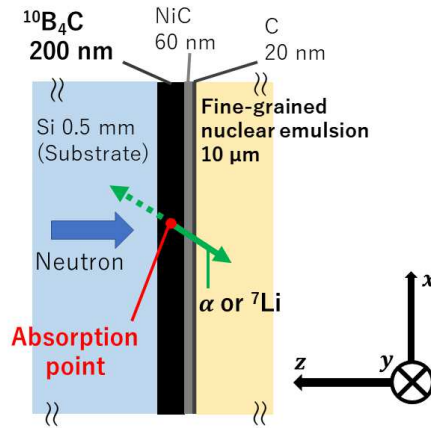


Figure 1. Schematic cross-sectional view of our high-resolution nuclear emulsion detector for cold neutrons and UCNs. Neutrons enter into the detector from the left. A $^{10}\text{B}_4\text{C}$ layer converts the neutrons to α -particles and ^7Li particles, emitted back-to-back. Both of these create a track in the emulsion on the right side.

The coordinates of the absorption points are obtained by the following eight steps. First, tomographic images are acquired by taking images at different heights in 63 steps distributed equally over the thickness of the emulsion layer. Each image has a field of view of $113 \mu\text{m} \times 113 \mu\text{m}$ and the resolution is 2048×2048 , resulting in a pixel size of $55 \text{ nm} \times 55 \text{ nm}$. The thickness of each imaging layer (corresponding to the vertical resolution) is $0.37 \mu\text{m}$ prior to shrinking of the emulsion during development. Second, pixels with low brightness values corresponding to silver particles are detected in the acquired images, and those pixels are recognized as a part of grains. This detection is performed twice: once for images that only contain real images and again for images containing the mirror images of the tracks. Third, grains in the lowermost 1.5 layers above the base layer are selected. These grains correspond to the starting points of tracks in the emulsion. Fourth, pairs of two grains corresponding to the starting and ending point of original tracks whose distance is consistent with the theoretical track length (more than $1.5 \mu\text{m}$ and less than $7.5 \mu\text{m}$) are assigned. If the density of original tracks is high, the starting or ending points of two or more

tracks may be mixed during the selection process. In this case, there are no silver particles on the three-dimensional straight line connecting the starting and ending points, which means that the total brightness value of the pixels on this line is higher than it should be for a real track. Fifth, to reject these pairs, if the distance between the starting points or ending points of different pairs is less than $0.8\ \mu\text{m}$, the pairs with the higher total brightness value are excluded. Sixth, for the remaining starting/ending point pairs having proper distances, tracks are reconstructed from the grains lying on the connecting line between the two points. These are called subsequently ‘reconstructed tracks’. Seventh, the coordinates of the point of the boundary between real and mirror images at the surface of the C layer, and the slopes of each reconstructed track are obtained by fitting both images of each track with symmetrical lines. Finally, absorption points of neutrons are identified by extrapolating the reconstructed track of the real images to the middle of $^{10}\text{B}_4\text{C}$ layer using the fitting results. The spatial resolution of this detector was calculated from the data of Reference [12] to be less than 100 nm. Note that we only consider tracks with angles $\theta \leq 0.9$ rad between the track and the normal line to the surface of the C layer, as for tracks at larger angles, the error increases significantly. The resolution obtained with the aforementioned procedure with our emulsion detectors is superior by more than one order of magnitude compared to other neutron detectors [2, 14].

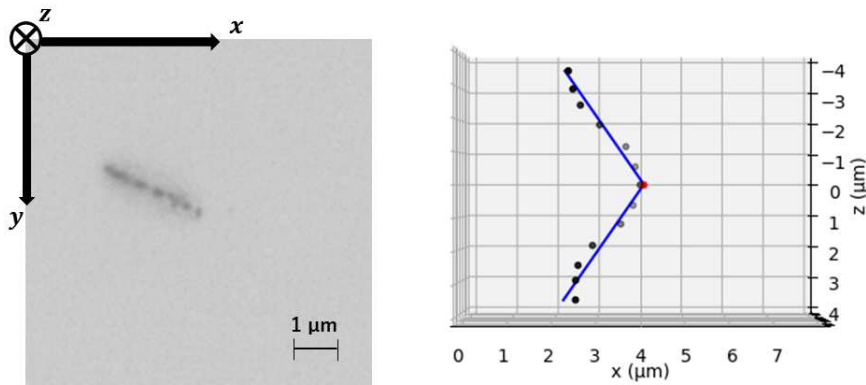


Figure 2. Track of an α -particle visible in an optical microscope image (left), and the reconstructed track in the x - z plane (right). Pixels with low brightness correspond to silver particles, which are recognized as grains. Right: Black dots show the grain coordinates reconstructed from the figure on the left. The blue line shows a reconstructed track obtained from fitting the grains. The red dot shows the coordinates of the point of the boundary between real and mirror images on the surface of the C layer ($z = 0$) resulting from the line fits.

In order to utilize the detector in the measurement of the spatial distribution of UCNs, two key issues had to be resolved. The first issue was to establish a method to ensure that high spatial accuracy and resolution in a detection area of $65\ \text{mm} \times 0.2\ \text{mm}$, where a field of view of the microscope is $113\ \mu\text{m} \times 113\ \mu\text{m}$. This cannot be guaranteed by simply stitching images from different positions, as offsets accumulate and lead to increasing errors. Therefore, we created microscopic marks on the Si substrate that serve as independent reference points to align the optical images. We demonstrated this method to work and the achievement of high spatial resolution by

an analysis of the transmission image of a gadolinium grating taken by cold neutrons at the Japan Proton Accelerator Research Complex (J-PARC). The second issue was to find a method allowing us to utilize the emulsion detector in a vacuum of 1 Pa or less environment. This was necessary, as measurements with UCNs have to be done under vacuum to prevent scattering of neutrons by compounds in the air. Therefore, we developed a holder that allows maintaining the volume around the emulsion at atmospheric pressure. Finally, a test exposure to UCNs was conducted at Institut Laue-Langevin to obtain the spatial distribution.

2 Improvements of the detector

In order to perform an actual measurement of the spatial distribution of UCNs, we assembled a new emulsion detector (see Figure 3) implementing all of the improvements mentioned above. We created circular reference marks of 1 μm and 5 μm diameter with an interval of $d_1 = 50 \mu\text{m}$ and $d_2 = 500 \mu\text{m}$, respectively, over an area of 65 mm \times 0.2 mm on the Si substrate using an electron beam lithography system (JBX-6300FS). Absolute coordinate values of the centers of the marks were determined with an accuracy better than 30 nm thanks to laser interferometers used to determine the position during the marking process. The depth of the marks was 500 nm. The marks were successfully recognized as black circles under the microscope as shown in Figure 4. These marks make it possible to define the entire analysis area in a unified coordinate system.

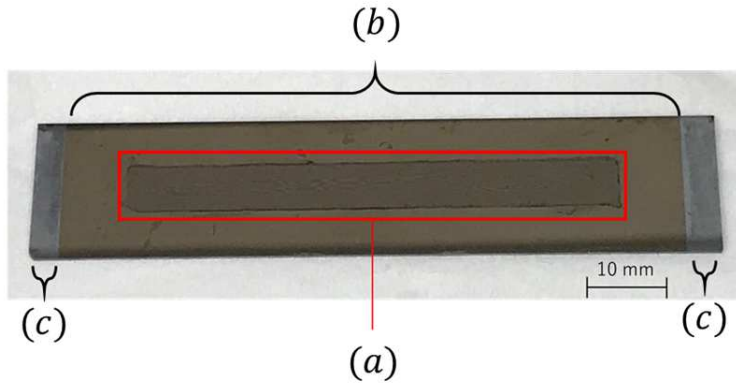


Figure 3. Detector used in the measurement of the spatial distribution of quantized UCNs. (a) – (c) indicate the following regions: (a) nuclear emulsion, (b) Si substrate and $^{10}\text{B}_4\text{C}$ -NiC-C layer, (c) plain Si substrate.

The coordinate values of neutron absorption points were converted from the coordinate system of each image to the unified coordinate system defined by the marks using an affine transformation as follows,

$$\begin{pmatrix} X_i \\ Y_i \\ 1 \end{pmatrix} = \begin{pmatrix} A & B & C \\ D & E & F \\ 0 & 0 & 1 \end{pmatrix} \begin{pmatrix} x_i \\ y_i \\ 1 \end{pmatrix}, \quad (2.1)$$

where the values of the i -th absorption point in the coordinate system of the image are (x_i pixel, y_i pixel), those in the unified coordinate system are ($X_i \mu\text{m}$, $Y_i \mu\text{m}$) as shown in Figure 5, and A , B , C ,

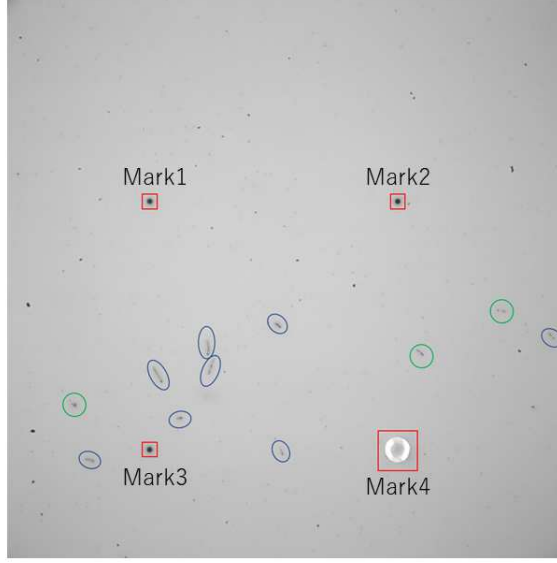


Figure 4. Tracks and reference marks on an optical microscope image. Reference marks have been highlighted by red squares. There are two different types of markings. Mark4 in the figure are $5\ \mu\text{m}$ in diameter and lie on a grid with $500\ \mu\text{m}$ spacing. All other marks (Mark1, Mark2, Mark3) in the figure are $1\ \mu\text{m}$ in diameter and lie on a grid with $50\ \mu\text{m}$ spacing. ${}^7\text{Li}$ nuclei and α -particles tracks are indicated by blue ellipses. Green circles indicate stains or tracks at large angles $\theta > 0.9$ rad, which are excluded from the analysis (see main text).

D , E , and F are affine transformation parameters. The parameters were acquired by the following formula using the information of three marks among four in each view:

$$\begin{pmatrix} A_j \\ B_j \\ C_j \end{pmatrix} = \begin{pmatrix} x'_j & y'_j & 1 \\ x'_k & y'_k & 1 \\ x'_l & y'_l & 1 \end{pmatrix}^{-1} \begin{pmatrix} d_1 M'_j \\ d_1 M'_k \\ d_1 M'_l \end{pmatrix}, \quad (2.2)$$

$$\begin{pmatrix} D_j \\ E_j \\ F_j \end{pmatrix} = \begin{pmatrix} x'_j & y'_j & 1 \\ x'_k & y'_k & 1 \\ x'_l & y'_l & 1 \end{pmatrix}^{-1} \begin{pmatrix} d_1 N'_j \\ d_1 N'_k \\ d_1 N'_l \end{pmatrix}, \quad (2.3)$$

where (j, k, l) are $(1, 2, 3)$, $(2, 3, 4)$, $(3, 4, 1)$, or $(4, 1, 2)$, and (x'_j, y'_j) are the center coordinates of the (M'_j, N'_j) -th mark in (x, y) directions, respectively, with respect to the origin of the unified coordinate system shown in Figure 5. A , B , C , D , E , and F are determined by the average of the A_j , B_j , C_j , D_j , E_j , and F_j obtained for all (j, k, l) pairs. We obtained the coordinate values of the marks in two steps. First, the edge of the mark was acquired using a Canny edge detector [15]. Then, the coordinates of the marks were obtained using a Hough transform [16] of the detected edge assuming that marks were circular. To avoid errors caused by distortion due to the microscope lens, the region inside the marks ($50\ \mu\text{m} \times 50\ \mu\text{m}$) was set to the center of each tomographic image and the region was called subsequently ‘view’. Tomographic images were acquired with an interval

of $50\ \mu\text{m}$ in the x - y plane. If deformed markers are created, the respective views are excluded from the analysis since the center coordinates of marks cannot be determined by a Hough transform.

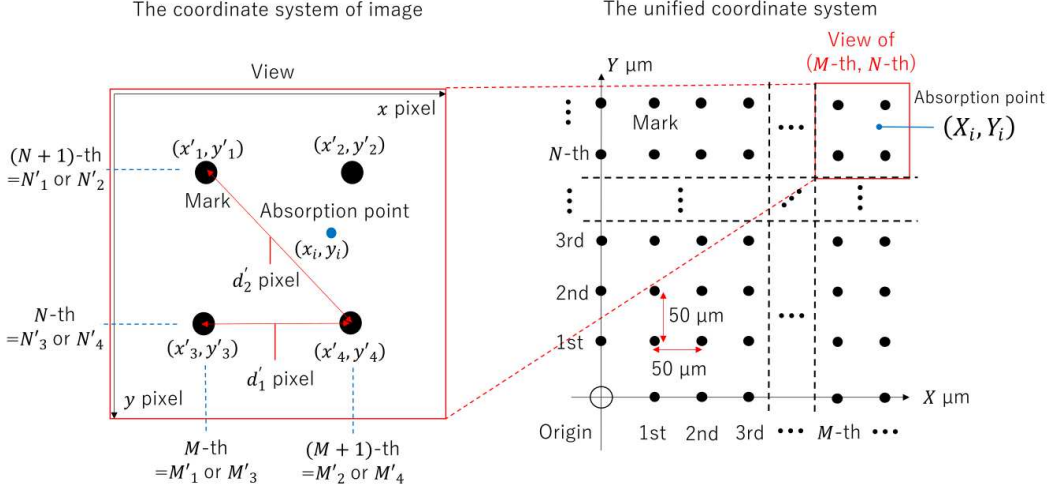


Figure 5. Schematic view of the image and unified coordinate systems. The black circles indicate reference marks. The blue dot represents an absorption point in both coordinate systems, whose values were $(x_i \text{ pixels}, y_i \text{ pixels})$ and $(X_i \mu\text{m}, Y_i \mu\text{m})$. The coordinates of the marks are $(x' \text{ pixel}, y' \text{ pixel})$, and the subscripts 1, 2, 3, and 4 refer to the upper left, upper right, lower left, and lower right of each view, respectively. M and N are the lattice indices in x and y directions, respectively, starting from the mark on the origin of the unified coordinate system. M'_1 or M'_3 corresponds to M . M'_2 or M'_4 corresponds to $M+1$. N'_3 or N'_4 corresponds to N . N'_1 or N'_2 corresponds to $N+1$.

The error of the transformation from the image coordinate system to the unified coordinate system depends on the error of the center coordinates of the marks. The error was estimated by measuring the distance between adjacent marks d'_1 pixel and those between diagonally adjacent marks d'_2 pixel were calculated from $(x' \text{ pixel}, y' \text{ pixel})$ (see Figure 5). Then, d'_1 pixel and d'_2 pixel were translated to $d_1 \mu\text{m}$ and $d_2 \mu\text{m}$, respectively, by using the fact that one pixel is equal to 55 nm . d_1 was measured for 400 marks and d_2 for 200 marks, resulting in average values $d_1 = 50.0010(19) \mu\text{m}$ and $d_2 = 70.7046(29) \mu\text{m}$ and standard deviations $\sigma_{d_1} = 38.3(14) \text{ nm}$ and $\sigma_{d_2} = 40.7(20) \text{ nm}$, obtained by fitting a Gaussian function to the histograms, respectively. Assuming the errors of the single mark coordinates to be equal, we divide the errors in $d_1 \mu\text{m}$ and $d_2 \mu\text{m}$, by $\sqrt{2}$ to estimate the errors of the mark center coordinates. Conservatively, using the larger value σ_{d_2} , we thus obtain the standard deviation of the center coordinates of the marks to be $28.8(14) \text{ nm}$. Note that this standard deviation includes not only the limited accuracy of determining the position of the marks during the electron beam lithography but also the accuracy of reading the coordinate values of the marks. The given value ($28.8(14) \text{ nm}$) is consistent with the specified accuracy (less than 30 nm) of our electron beam lithography equipment.

The second issue solved by the new detector relates to measurements in a vacuum environment. If the nuclear emulsion would be exposed to a vacuum, the contained water would disperse quickly,

causing cracking and peeling of the emulsion surface. The torsion would further lead to an increase in silver grains not related to tracks that would be recognized as noise (fog) in the image. To operate the emulsion in a vacuum nonetheless, we developed a holder to maintain the volume around it at atmospheric pressure (Figure 6). The central part of the top cover was hollowed out in an area of 10 mm × 80 mm to prevent scattering of incident ultracold neutrons at the holder. The nuclear emulsion gel was applied to the central area of 7 mm × 65 mm to prevent contact with the holder. We conducted a durability test by placing a nuclear emulsion in this holder under a vacuum of 3×10^{-3} Pa for two days, corresponding to a typical duration for an exposure with ultracold neutrons. Subsequently, the state of the nuclear emulsion was confirmed with an optical microscope after development. Neither cracks nor the increase of fog was observed on the surface of it, which confirms that the holder serves its purpose.

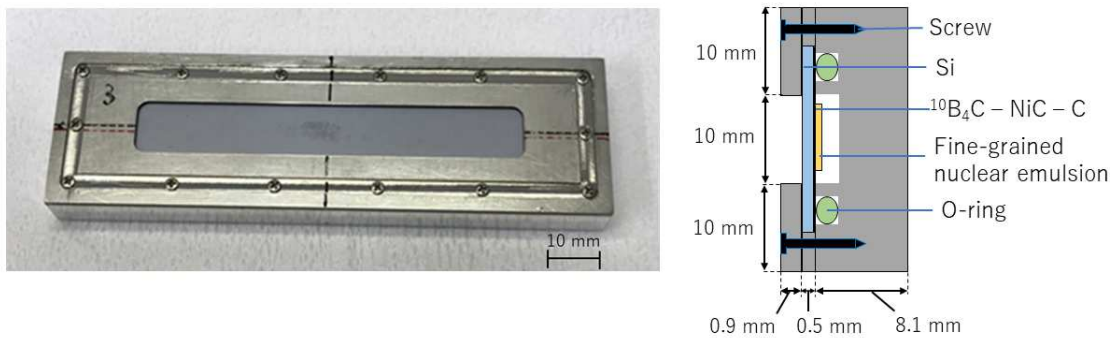


Figure 6. Holder allowing in-vacuum use of the emulsion detector. (left: photograph of the holder, right: schematic view of its cross section). The central part of the top cover of the holder was hollowed out to allow direct exposure of the surface of Si to vacuum. The yellow part of the schematic view shows the nuclear emulsion layer; the volume around it is kept at atmospheric pressure.

3 Measurement of the resolution using a gadolinium grating

The spatial resolution of the improved detector was evaluated by acquiring a transmission image of a neutron-absorbing Gd grating that has a periodic structure along the X -axis direction (see Figure 7) and creates a sharp shadow on the detector. Subsequently, the edges of the shadow were numerically analyzed by fitting the profile with an error function. This experiment was conducted at BL05 [17, 18] of the Materials and Life Science Experimental Facility in J-PARC using cold neutrons of approximately 1000 m/s. The 12 μm thick grating was created by vapor deposition of Gd from an oblique angle on a Si mold with a comb-like structure of period of 9.00 μm (measured by confocal microscopy), and the opening of the Gd grating was 4 μm [19]. Figure 8 shows an electron micrograph of the cross section of a similar Gd grating made by the same process. A nuclear emulsion wrapped with two aluminum foils with a total thickness of 20 μm for light shielding was placed behind the Gd grating. The detector was then exposed through the Gd grating for 2.0×10^4 s using cold neutrons (Figure 7) with a beam flux of 7.6×10^4 neutrons/cm²/s, as measured with a ^3He proportional counter. We estimated the transmittance of the 12 μm Gd layer to be 2%, which

can be ignored. Due to the geometric view factor given by the Gd grating, one-third of the total beam reached the detector. From the total number of impeding neutrons, and the track count on the detector we determined a detection efficiency of 0.50%. This corresponds well to the theoretical estimate 0.65% (corresponding to 3.3×10^2 tracks per $100 \mu\text{m} \times 100 \mu\text{m}$) based on the thickness of the $^{10}\text{B}_4\text{C}$ layer. The beam divergence angle was 5.6×10^{-2} mrad and 0.56 mrad in the X -axis and Y -axis direction, respectively.

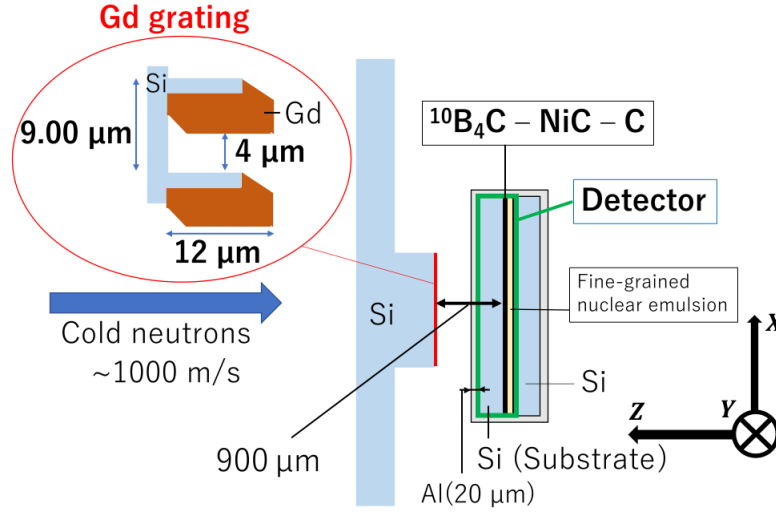


Figure 7. Setup for the measurement of cold neutron detection resolution. The Gd grating is located on the downstream side of a Si-slab placed in front of the detector. A Si plate was inserted to separate the emulsion layer from the Al foil to avoid the chemical effects of Al on the emulsion.

Figure 10 shows an image of the detector taken with an optical microscope after development, in which the striped distribution of tracks can clearly be seen. We acquired the absorption points using the analysis method explained in Section 1. The reconstructed tracks were classified into four types: ‘Track’, ‘Track+Track’, ‘Track+Dust/Fog’, and ‘Dust/Fog’ as shown in Figure 9. ‘Track’ means that all grains belong to an original track. ‘Track+Track’ is an erroneously reconstructed track that consists of grains originally belonging to different tracks. ‘Track+Dust/Fog’ means that some grains of the track are fog or dust origin. ‘Dust/Fog’ means that all grains are dust or fog origin. The types other than ‘Track’ were treated as noise. Since the grains of a track that was categorized as noise are not distributed on a straight line, it is considered that the χ^2/ndf of the corresponding line fit is increased with respect to a regular track. Therefore, the noise contamination rate can be reduced by not using reconstructed tracks with a large value of χ^2/ndf in the analysis. χ^2 was acquired by the following formula,

$$\chi^2 = \sum_i \left(\left(\frac{\delta R_i}{\delta a \sqrt{1 + \left(\frac{\delta b}{\delta a} \right)^2 \tan^2 \theta}} \right)^2 + \left(\frac{\delta L_i}{\delta a} \right)^2 \right), \quad (3.1)$$

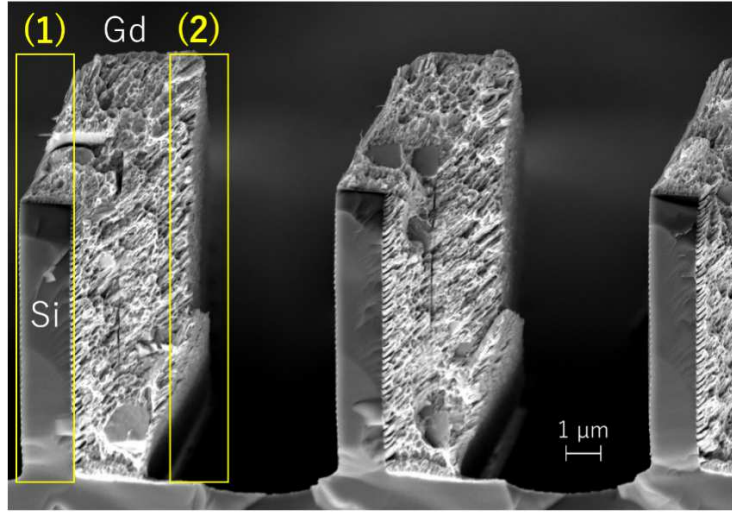


Figure 8. Electron micrograph showing a cross section of a Gd grating that was manufactured by the same process as that used in this experiment. The thickness of Gd in (1) is not sufficient to prevent cold neutrons from passing. We used the transmission image of the edge (2) for the estimation of the resolution of the detector.

where

$$\begin{pmatrix} \delta R_i \\ \delta L_i \end{pmatrix} = \begin{pmatrix} \cos \phi & \sin \phi \\ -\sin \phi & \cos \phi \end{pmatrix} \begin{pmatrix} x_t(z_i) - x_i \\ y_t(z_i) - y_i \end{pmatrix}. \quad (3.2)$$

Here, θ and ϕ are the angle of a track in a spherical coordinate system, the coordinates of the i -th grain are (x_i, y_i, z_i) , those of the reconstructed track at z_i are $(x_t(z_i), y_t(z_i))$, $\delta a = 57$ nm is the standard deviation in the δL_i direction, and $\delta b = 300$ nm is the standard deviation in the z direction. In order to systematically remove noise from our data, we introduce the empirical criterion $\chi^2/\text{ndf} < 2$. This cutoff value was determined by analyzing the typical χ^2/ndf for reconstructed tracks belonging to the four categories described above (see also Figure 9). For this purpose, we randomly selected 20 reconstructed tracks and classified them according to their respective χ^2/ndf as shown in Table 1. The number of survived tracks after applying the cutoff was 3022.

Table 1. Classification of 20 randomly selected reconstructed tracks according to their χ^2/ndf , used to empirically set the threshold for acceptance $\chi^2/\text{ndf} < 2$. These tracks were visually checked and classified as described in the main text.

χ^2/ndf	0.00 – 0.67	0.67 – 1.33	1.33 – 2.00	2.00 – 2.67
Total events	939	1267	816	529
Track	17	16	14	5
Track+Track	1	2	3	10
Track+Dust/Fog	2	0	2	5
Dust/Fog	0	2	1	0
Checked tracks	20	20	20	20

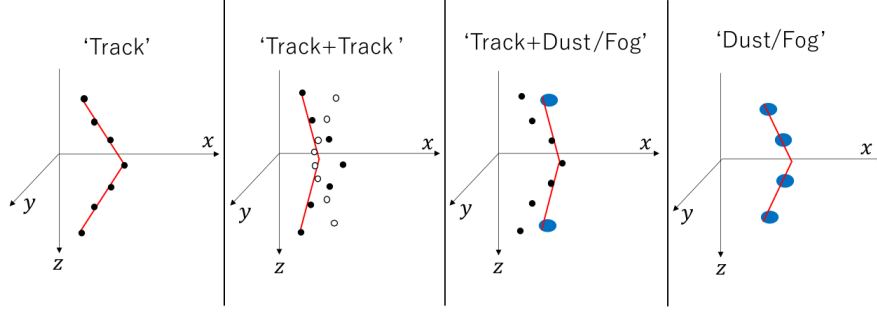


Figure 9. Classification of the reconstructed tracks. The reconstructed tracks were classified into four types. Red lines show reconstructed tracks. Black dots show silver particles. White dots of ‘Track+Track’ show silver particles on a track originally belonging to a different track than that of black dots. Blue ellipses of ‘Track+Dust/Fog’ or ‘Dust/Fog’ show fog or dust.

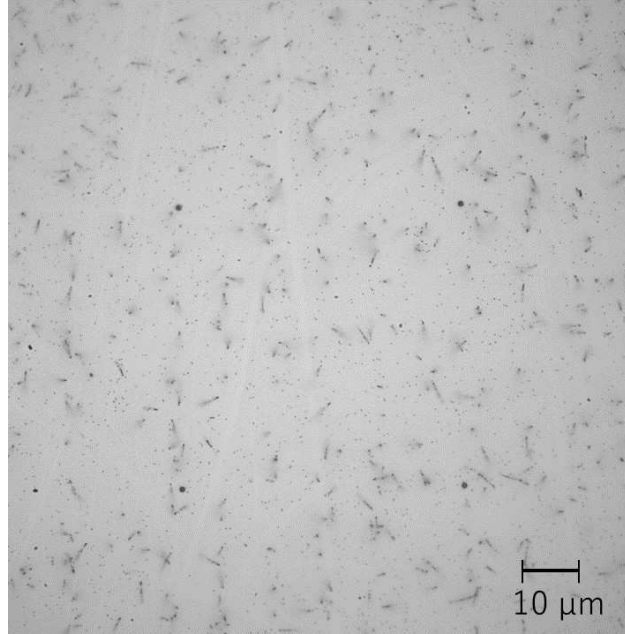


Figure 10. Transmission image of Gd grating.

The distribution of the length of survived tracks used in the analysis is shown in Figure 11. The analyzed region was $500 \mu\text{m} \times 500 \mu\text{m}$, and the coordinates of the absorption points obtained in each view was converted into the unified coordinate system using Equation 2.1. Figure 12 shows a plot of the absorption points. A striped pattern corresponding to that of the structure of the Gd grating can be observed in the plot, as expected. In order to remove an overall tilt angle α and determine the period d of the pattern, we use the Rayleigh test function $R(\alpha, d)$ [20, 21]:

$$R(\alpha, d) = \frac{2}{N} \left(\left(\sum_i \sin \left(\frac{2\pi x_i(\alpha)}{d} \right) \right)^2 + \left(\sum_i \cos \left(\frac{2\pi x_i(\alpha)}{d} \right) \right)^2 \right), \quad (3.3)$$

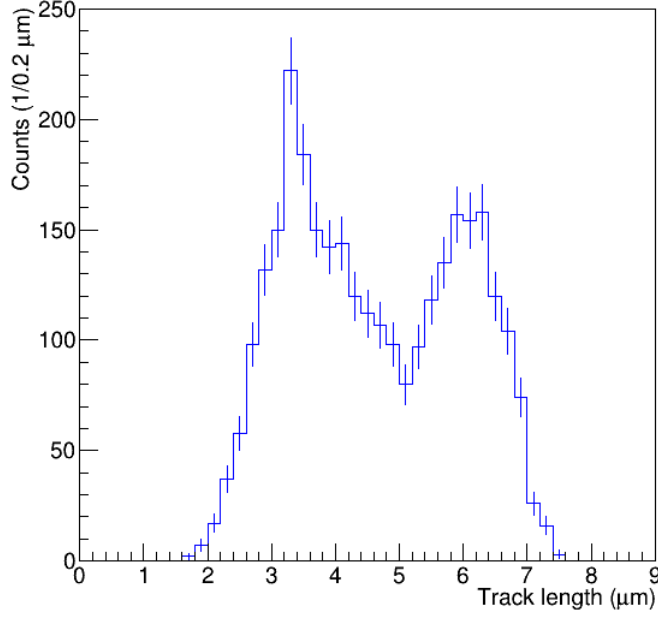


Figure 11. Distribution of the length of survived tracks in the analysis. The figure shows the length from the absorption points to the ending points of the grain, assuming the absorption reaction happens in the middle of the thickness of $^{10}\text{B}_4\text{C}$ layer. The two peaks of the distribution correspond to ranges of tracks of ^7Li nuclei and α -particles with theoretical center values of $2.7(4) \mu\text{m}$ and $5.2(4) \mu\text{m}$ in the emulsion, calculated by SRIM-2013, respectively. Slight differences from the calculated values are explained with the error of the shrinkage rate of the emulsion layer during the development.

where

$$x_i = X'_i \cos \alpha + Y'_i \sin \alpha + x_m, \quad (3.4)$$

and

$$\begin{pmatrix} X'_i \\ Y'_i \end{pmatrix} = \begin{pmatrix} X_i - x_m \\ Y_i - y_m \end{pmatrix}. \quad (3.5)$$

Here, N is the total number of absorption points, (X_i, Y_i) are the coordinates in the unified coordinate system [c.f. Equation 2.1], and (x_m, y_m) are the average values of the coordinates of all absorption points. Optimum values $\alpha_m = -1.623(30) \times 10^{-2}$ rad and $d_m = 8.9997(26) \mu\text{m}$ were obtained by maximizing $R(\alpha = \alpha_m, d = d_m)$ numerically. The detected period is consistent with the designed value of the Gd grating, $9.00 \mu\text{m}$.

Subsequently, the tilt was removed from the data by rotating coordinates by $-\alpha_m$ using Equation 3.4. The histogram of the distribution of the absorption points folded with the period of d_m , i.e., x_i modulo d_m , is given in Figure 14. A peak corresponding to the opening of the Gd grating was observed from 3.5 to $7.0 \mu\text{m}$. In addition, it was understood that the part from 4 to $5 \mu\text{m}$ corresponded to (1) in Figure 8 because the number of events from 4 to $5 \mu\text{m}$ of the horizontal axis in Figure 14 was smaller than the number of events from 5 to $6 \mu\text{m}$. The transmission image corresponding to (1) is more blurred than that corresponding to (2) since the thickness of Gd in (1)

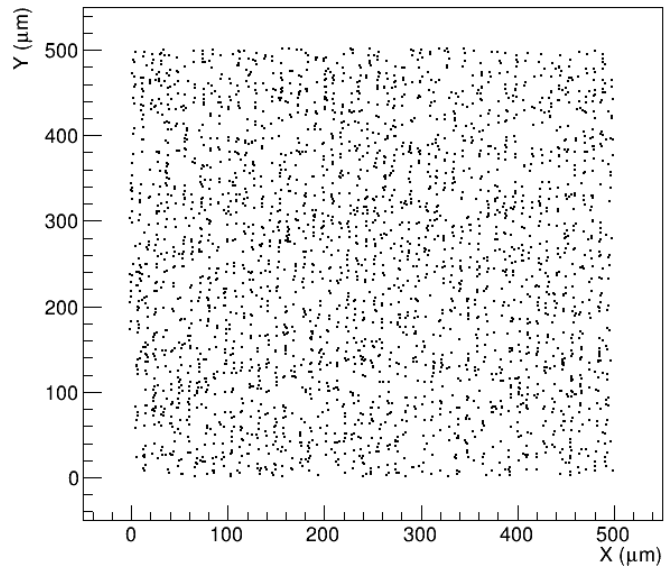


Figure 12. Distribution of absorption points of neutrons that passed through the Gd grating.

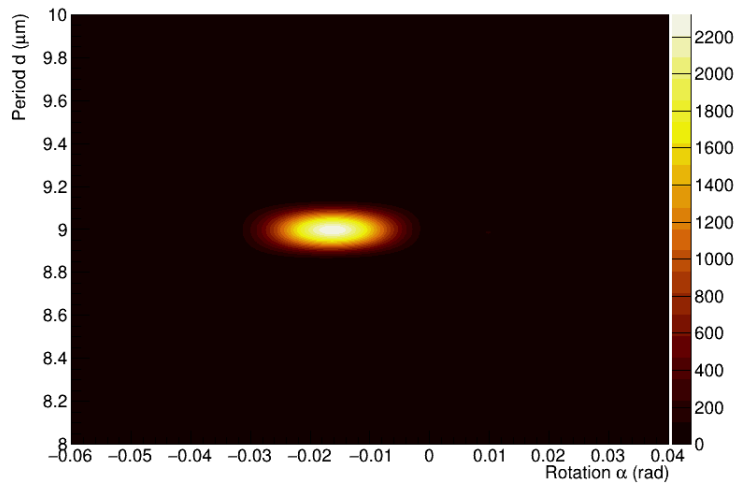


Figure 13. Results of the Rayleigh test. The color coding expresses the value of the Rayleigh test function $R(\alpha, d)$. The brightest R point indicates the optimum values of α and d .

is not sufficient. Therefore, we did not use the left side of the transmission image but the right side of it. We fitted the right edge of the data in Figure 14 with the error function:

$$f(x) = A \left(\frac{1}{\sqrt{2\pi}\sigma} \int_x^\infty \exp\left(-\frac{(t-\mu)^2}{2\sigma^2}\right) dt \right) + B, \quad (3.6)$$

where μ μm is the coordinate of the edge of a stripe on the detector, σ μm is the effective blurring of the distribution, A is a scaling factor of the distribution, and B is the amount of background noise. All of the mentioned variables were used as free parameters of the fit. Since the cross section of the sputtered Gd layer is not a perfect rectangle as shown in Figure 8, it is assumed that σ becomes larger than a certain value. Assuming that all Gd shapes are the same as in Figure 8, the thickness distribution can be obtained from the figure. The lower limit of σ was $0.14 \mu\text{m}$ by fitting the transmission image estimated from the thickness distribution with Equation 3.6. The fitting result is shown in Figure 15. We obtain a spread of $\sigma = 0.56(8) \mu\text{m}$, which includes the effects of the intrinsic resolution of the detector, the accuracy of the connecting of views using the reference marks, the spread of the beam, the shape of the Gd grating, and the variation in the amount of Gd on each Si mold. It is therefore reasonable to state that the intrinsic resolution of the detector is expected to be better than the given value. The divergence angle of the beam in the x -axis direction (horizontal axis in Figure 14) was obtained by rotating the original divergence angle by $-\alpha_m$. The maximum value was 6.5×10^{-2} mrad. The distance between the Gd grating and the $^{10}\text{B}_4\text{C}$ layer of the detector was $900 \mu\text{m}$; hence, the spread of the transmission image due to the divergence angle was 60 nm . It was considered that probably the variation in the amount of Gd on each Si mold was dominant for the value of the resolution.

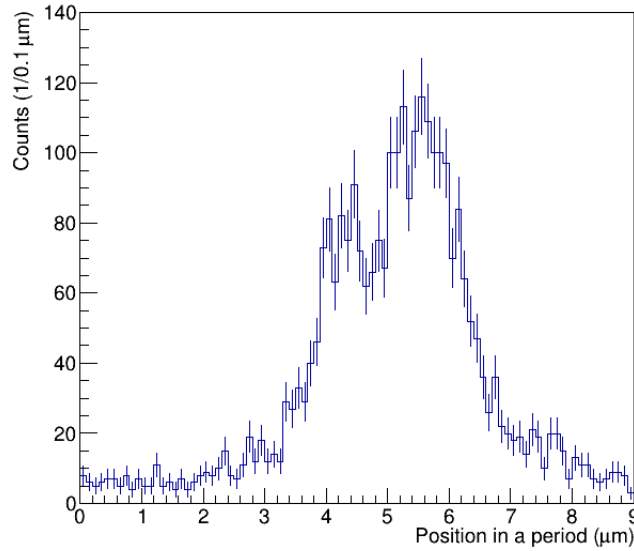


Figure 14. Distribution of x_i modulo d_m in the Gd transmission measurement. The resolution of the detector was evaluated using x_i modulo $d_m > 5.0 \mu\text{m}$ whose region corresponded to the sharp edge of Gd grating.

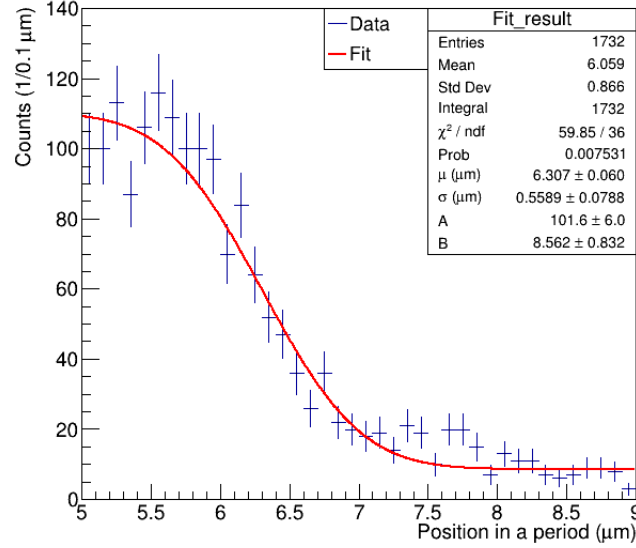


Figure 15. Fit result of the absorption points around the Gd grating edge. The blue histogram data is an excerpt of the data in Figure 14 for x_i modulo $d_m > 5.0 \mu\text{m}$. The red line shows the result of the least squares fit of Equation 3.6 to the data.

4 Measurement of the spatial distribution of quantized UCNs

As a demonstration of our emulsion detector, we attempted to measure the spatial distribution of UCNs that take quantized states in the potential well created between the Pseudo-Fermi potential of a horizontal flat mirror and the gravitational potential of the Earth, a system commonly known as ‘quantum bouncer’ [22]. This experiment was conducted at PF2 of the Institut Laue-Langevin. The experimental setup is shown in Figure 16. A combination of a flat mirror with a rough absorber/scatterer on top, separated by precision spacers of nominal thickness $30 \mu\text{m}$ creates a selector for vertical energy states of neutrons [23]. Neutrons colliding with the rough upper surface are scattered and absorbed. The probability of this removal of neutrons from the system is proportional to the overlap of the wave function with the rough surface of the upper absorber/scatterer. The slit width is chosen such that this overlap is practically zero for the ground state, and large for higher, unwanted states. At the exit of the selector, neutrons arrive in a well-defined superposition of quantum states that can be computed analytically. The mirror, absorber/scatterer and vacuum chamber in Figure 16 were taken from the *qBOUNCE* experiment [3]. Both the flat mirror and the rough absorber/scatterer are made of borosilicate glass. The size of the mirror was 15 cm and 20 cm in the Z - and X -axes, respectively. The size of the absorber/scatterer was 15 cm and 10 cm in the Z -axis and the X -axis directions, respectively. All parts of the setup were installed in a vacuum chamber, and the detector was exposed with UCNs for 16 hours in a vacuum of 1 Pa or less, where the scattering by air can be neglected. The beam flux was estimated to be 0.21 neutrons/s for the region exposed to neutrons from an actual measurement using a gas detector with a ^{10}B layer [5]. The velocity distribution of the UCNs was measured using an aperture system as shown

in Figure 17. Two plates of borated Al create a slit at horizontal and vertical distances w and h , respectively. The slit together with the gap between the absorber/scatterer and flat mirror define a flight parabola that selects the horizontal velocity v according to

$$v = \sqrt{\frac{gw^2}{2h}}, \quad (4.1)$$

where g is the gravitational acceleration. The velocity distribution was measured by varying h and counting the admitted UCNs by a gas detector as shown in the left of Figure 17. The result of this measurement is plotted on the right of Figure 17 and shows an almost Gaussian distribution with a mean of 9.53 m/s and a standard deviation of 2.18 m/s.

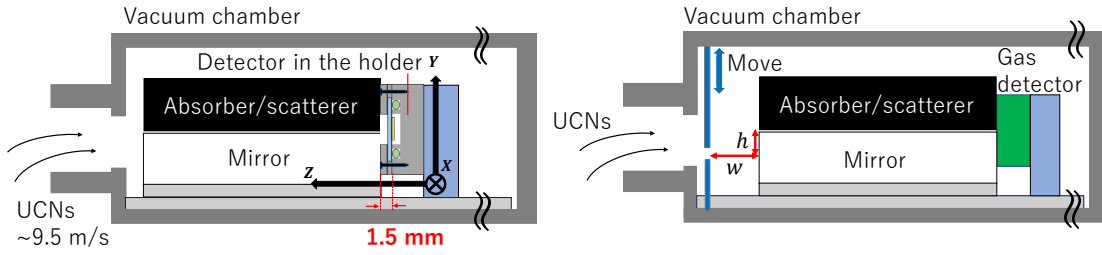


Figure 16. Setup for obtaining the quantized spatial distribution of UCNs. The figures on the left and right show the schematic view of the setup of the measurement of coordinates and velocity of UCNs, respectively. The distance from the exit of the mirror and absorber/scatterer to $^{10}\text{B}_4\text{C}$ layer is 1.5 μm .

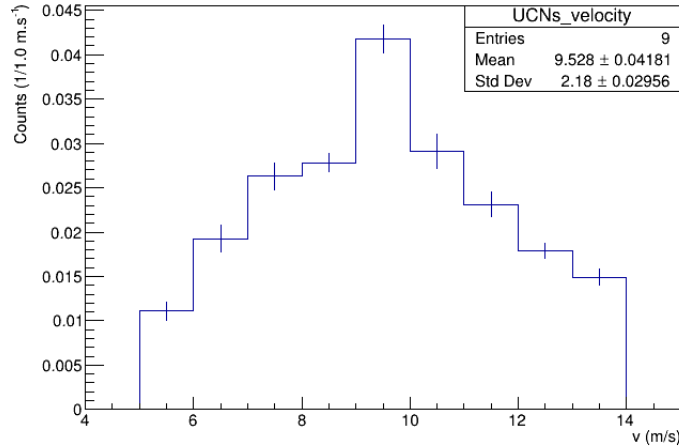


Figure 17. Measured velocity distribution at the UCN beam of the PF2 installation. The counts of UCNs of 4 – 11 m/s were measured using a gas detector with a ^{10}B layer.

We reconstructed the tracks and classified them as explained in Section 3. The result of the classification and the number of total events are summarized in Table 2. The reason for the noise

contamination rate here being lower than in the analysis of Gd grating is that the tracks are less likely to overlap in this measurement due to the smaller density of tracks on the detector.

Figure 18 shows the distribution of the scanned area and the absorption points (red) of neutrons. The area shown in light blue in Figure 18 shows the scanned region; green indicates areas that were excluded due to difficulties in the recognition of marks due to deformed reference marks or the presence of large dust particles on the surface of the C layer. The scanned area was 65 mm and 0.2 mm in the directions of the X - and Y -axes, respectively. The excluded area was 2.7 % of the scanned area. We restricted our analysis to absorption points inside the purple lines, containing a total of 1821 tracks.

Table 2. Classification of 20 randomly selected reconstructed tracks depending on their χ^2/ndf . These tracks were visually checked and classified as described in the main text.

χ^2/ndf	0.00 – 0.67	0.67 – 1.33	1.33 – 2.00	2.00 – 2.67
Total events	729	830	314	175
Track	20	20	19	14
Track+Track	0	0	0	0
Track+Dust/Fog	0	0	0	1
Dust/Fog	0	0	1	5
Checked tracks	20	20	20	20

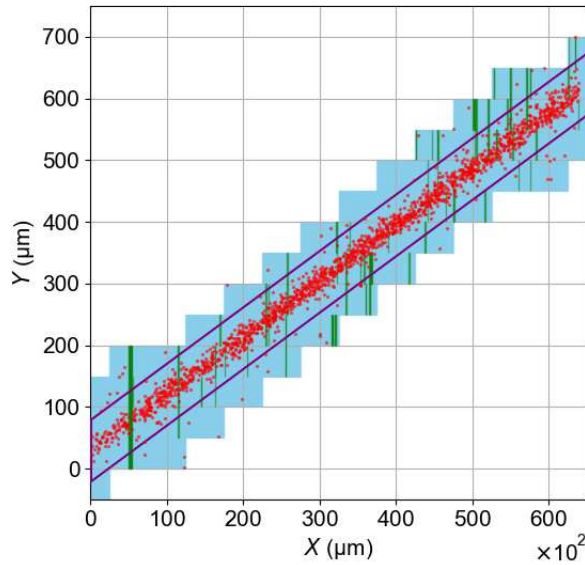


Figure 18. Scanned area and the distribution of absorption points. The length of the vertical axis is 1/100 of the length of the horizontal axis.

The obtained line of absorption points was slightly tilted with respect to the horizontal axis

as shown in Figure 18, due to the setting accuracy of the detector. From the least squares fit of the coordinates to a linear function, we obtained a rotation of 9.146(17) mrad and a small vertical offset that both were removed from the data. We created a histogram of the data along the vertical y direction shown in Figure 19, where the effect of the excluded area was considered. We compared the obtained distribution with the theoretical curve to verify the precision of the measurement and estimate the ratio of each quantum state. Neutrons bound by the pseudo-Fermi potential V_F of a horizontal surface from below and the gravitational potential mgy rising linearly with the distance y above the surface obey the Schrödinger equation [22]

$$E\psi(y) = \left(-\frac{\hbar^2}{2m} \frac{\partial^2}{\partial y^2} + mgy + V_F \Theta(y_s - y) \right) \psi(y), \quad (4.2)$$

where ψ is the wave function, y_s is the vertical coordinate of the mirror surface, m is the mass of a neutron, E is the energy of the system, \hbar is the reduced Planck constant, and g is the gravitational acceleration. Since V_F is several orders of magnitude larger than the neutron's kinetic energy in the vertical direction, we can safely assume the boundary condition

$$\psi(y = y_s) = 0, \quad (4.3)$$

for which neutrons cannot enter the mirror. The same is true for the rough surface of the absorber/scatterer. However, due to the stochastic roughness of this surface, an effective gap size d_e has to be considered at this boundary,

$$\psi(y = y_s + d_e) = 0. \quad (4.4)$$

When Equation 4.2 is solved under the boundary conditions of Equation 4.3 and 4.4, the eigenfunction of the n -th state can be written as,

$$\psi_n(y) = C_n \text{Ai}(Y_n(y)) + D_n \text{Bi}(Y_n(y)), \quad (4.5)$$

where

$$y_0 = \left(\frac{\hbar^2}{2m^2g} \right)^{\frac{1}{3}}, \quad (4.6)$$

$$E_0 = mgy_0, \quad (4.7)$$

and

$$Y_n = \frac{y}{y_0} - \frac{E}{E_0}. \quad (4.8)$$

Here, Ai and Bi denote the Airy functions, C_n and D_n are normalization constants. As reported in prior experiments [24], we found that neutrons with high vertical energies interact with the upper rough surface, where they are absorbed or upscattered – and accordingly removed from the measurement. Consequently, only a superposition of the lowest few energy eigenstates is observed in the detector.

For the evaluation of our experiment, we also need to consider the time evolution during free fall because the distance from the exit of the absorber/scatterer to the $^{10}\text{B}_4\text{C}$ layer of the detector was $\ell_0 = 1.5$ mm (see Figure 16). Suppose that the n -th wave function at the exit of the mirror and

absorber/scatterer is the initial state $\psi_n(y, t = 0)$, then the wave function reaching the $^{10}\text{B}_4\text{C}$ layer can be computed from [25],

$$\psi_n(y, t) = \int K(y, y', t) \psi_n(y', t = 0) dy', \quad (4.9)$$

where

$$K(y, y', t) = \sqrt{\frac{m}{2\pi\hbar t}} \exp\left(\frac{i}{\hbar} S(y, y', t)\right) \quad (4.10)$$

and

$$S(y, y', t) = \frac{m}{2t} \left(y' - y - \frac{1}{2}gt^2\right)^2 + mgyt - \frac{1}{6}mg^2t^2. \quad (4.11)$$

Here, $t = l_0/v$, v is the horizontal velocity of the neutrons.

In order to compare our theoretical prediction based on Equation 4.9 with our measurements, we used two different models: an ideal function with infinitely high spatial resolution, and a realistic function with finite resolution. The first model is given by the following expression as the maximum number of the quantum state was N :

$$f_1(y) = A \sum_{n=1}^N \left(P_n |\psi_n(y - y_s, t)|^2 \right) + B, \quad (4.12)$$

where A is the magnification of the distribution, B is the amount of background noise, and P_n is the relative probability of quantum state n obeying $\sum_{n=1}^N P_n = 1$. In Equation 4.12, the effects of interference terms are ignored, which is reasoned by these terms becoming extremely small on average due to the random phase of each neutron. The second model is as given by the following function with the finite resolution entering via a convolution with a Gaussian function in Equation 4.12:

$$f_2(y) = A \sum_{n=1}^N \left(\frac{P_n}{\sqrt{2\pi}\sigma} \int_{-3\sigma}^{3\sigma} |\psi_n(y - y_s - y'', t)|^2 \exp\left(-\frac{y''^2}{2\sigma^2}\right) dy'' \right) + B, \quad (4.13)$$

where σ represents the blurring of the distribution.

Both models were then used in the least squares fits to the histogrammized data from our measurement. For f_1 , we used A , B , and y_s as free parameters. For f_2 , σ was kept as additional free parameter. N and d_e were varied by hand but kept fixed for each fit. The true value of the effective gap d_e was assumed to lie between $26\ \mu\text{m}$ and $36\ \mu\text{m}$, considering the measured value of the gap and the effect of the roughness. We performed fits with the values $d_e = 26, 31,$ and $36\ \mu\text{m}$. For N , we initially restricted ourselves to the most probable cases $N = 3$ and $N = 4$. Generally, for $N = 4$, the probability P_4 of the state $n = 4$ becomes almost zero (except for the case of $d_e = 26\ \mu\text{m}$). In the latter case, P_4 was the largest of all states, which we consider an artifact caused by fixing d_e to a value far from the real one. Therefore, the number of states was fixed to be $N = 3$ in all subsequent fits.

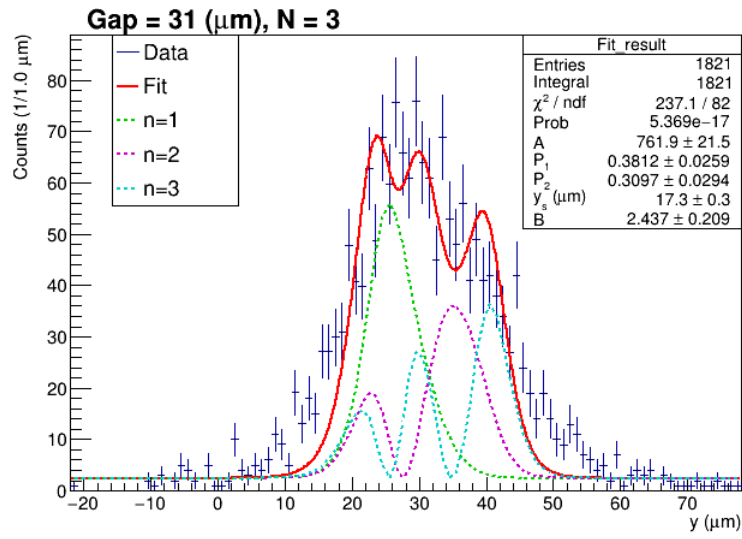


Figure 19. Fit result using the model in Equation 4.12, which neglects blurring. The effective gap was fixed to 31 μm and the maximum number of the quantum state was 3. The blue histogram shows the distribution of obtained absorption points. The red line shows the best fit result obtained with model $f_1(y)$. Dashed lines in green, purple, and light blue show the fitted probability distributions of the ground state, the first excited state, and the second excited state, respectively.

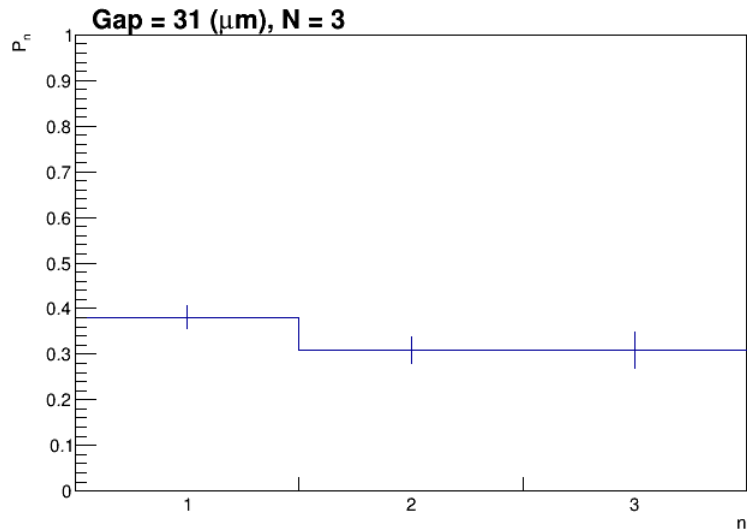


Figure 20. Relative probabilities of each quantum state for the fit result shown in Figure 19.

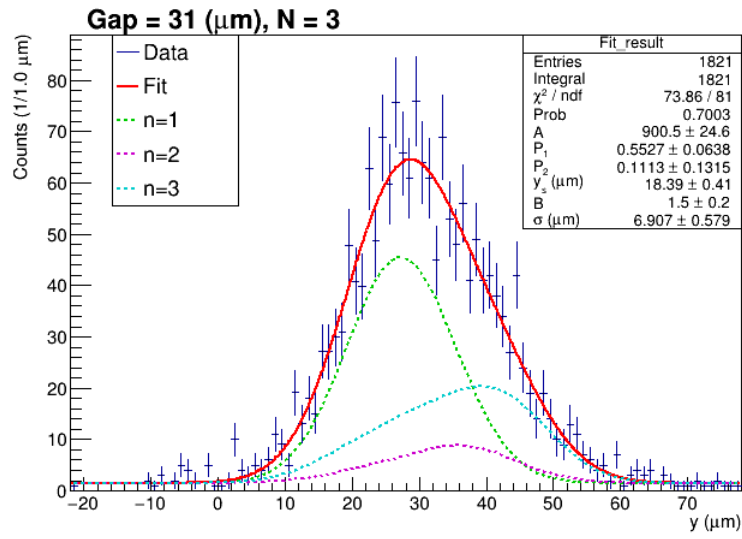


Figure 21. Fit result using Equation 4.13, which includes the effect of blurring. The effective gap was fixed to 31 μm and the maximum number of the quantum state was 3. The blue histogram shows the distribution of obtained absorption points. The red line shows the best fit result obtained with model $f_2(y)$. Dashed lines of green, purple, and light blue show the probability distributions of the ground state, the first excited state, and the second excited state, respectively.

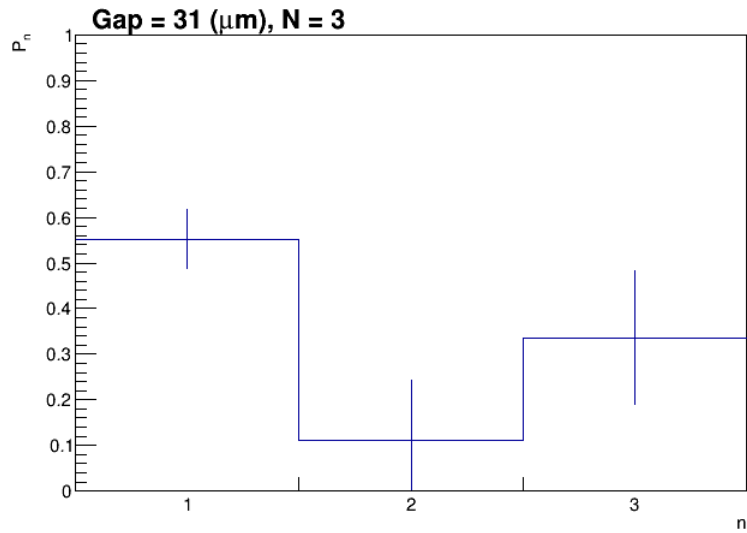


Figure 22. Relative probabilities of each quantum state for the fit result shown in Figure 21.

Figure 19 shows the fit results and the contributing probability distributions for each quantum state using the model y_1 for fixed effective gap was $d_e = 31 \mu\text{m}$. The relative probability of each state together with the respective parameter errors obtained from the fits are shown in Figure 20. The fit resulted in an extremely small p -value of 5.4×10^{-17} , indicating low statistical probability that the model without consideration of blurring represents the data well.

Figure 21 and Figure 22 show the respective fit results and the relative of each quantum state, for the same fixed parameters but using the model y_2 , which considers blurring. The best fit with p -value 0.70 was obtained for $\sigma = 6.9 \mu\text{m}$, indicating a valid result. The accuracy of determining the probability of each quantum state was lowered due to this blurring.

The cause of the difference in resolution between cold neutrons (used for the measurements with the Gd grating) and UCNs was considered to be the effect of neutron refraction due to the large surface roughness of the upstream (beam side) of the Si substrate in front of the emulsion layer. The refraction was negligible at the downstream side (emulsion side) of Si substrate as the surface roughness was polished. To evaluate this effect, we measured the height of the roughness $z(x, y)$ of the surface of the Si substrate within a $560 \mu\text{m} \times 560 \mu\text{m}$ region with an interval of $2 \mu\text{m}$, where z is a coordinate value in the direction of the thickness of the substrate, using a 3D Optical Profiler (Zygo NewView 6000). From the results, we obtained a set of values,

$$g(x, x', y) = \langle (z(x, y) - z(x', y))^2 \rangle, \quad (4.14)$$

as discussed in Reference [26]. For the estimation of the blur described below, we followed the procedure outlined in Reference [27]. Then, the set was transformed to $g'(r)$, where $r = \sqrt{x^2 - x'^2}$ is the absolute distance between two measurement points. Finally, $g'(r)$ was fitted by the following function,

$$f(r) = 2b^2 \left(1 - \exp \left(- \left(\frac{r}{\sqrt{2}w} \right)^2 \right) \right), \quad (4.15)$$

where b and w are the standard deviation of the surface roughness and the correlation length, respectively. From the fit results, we obtained $b = 0.293(6) \mu\text{m}$ and $w = 3.44(20) \mu\text{m}$. For these values, the classical refraction effect is dominant for UCNs. Assuming that the neutrons hit the silicon surface at normal incidence, the refraction angle can be computed:

$$\theta = \frac{b}{\sqrt{2}w} \frac{k_s^2}{k_n^2}, \quad (4.16)$$

Using the values $k_n = 0.15 \text{ nm}^{-1}$ for the wavenumber of the neutrons for a mean velocity $v = 9.5 \text{ m/s}$, and $k_s = 0.051 \text{ nm}^{-1}$ for the critical wavenumber of Si, and we arrive at $\theta = 6.9 \text{ mrad}$. The resulting blur (spread of the waveform) for our Si substrate having a thickness of 0.5 mm is $3.4 \mu\text{m}$. In the case of the resolution measurement using the transmission image of the Gd grating, the typical velocity of cold neutrons used in the measurement was 1000 m/s and the wavenumber was 16 nm^{-1} ; hence, the refraction angle was $0.62 \mu\text{rad}$ and the blur was 0.31 nm . The magnitude of the latter blur was negligible compared to the resolution of the detector. Thus, the observed difference of the measured resolution between cold neutrons and UCNs can be explained quantitatively.

For all detectors used in the present investigation, the silicon surface on the downstream side (nuclear emulsion side) was polished. We measured the respective roughness within a $280 \mu\text{m} \times 280 \mu\text{m}$

region with an interval of $1\ \mu\text{m}$ in the same way as described above, and obtained $b = 0.60(4)\ \text{nm}$ and $w = 42(8)\ \mu\text{m}$. If b and w of the upstream side would be the same as the downstream side, the refraction angle would only be $1.2\ \mu\text{rad}$ from Equation 4.16, resulting in a blur of $0.58\ \text{nm}$ for a thickness of $0.5\ \mu\text{m}$ of the Si substrate. In addition, it was necessary to consider the spread of the distribution due to small-angle scattering, as the surface was polished. According to the micro-roughness model, the scattering intensity depends on the scattering angle θ as shown in Figure 23. The peak of the scattering angle due to small-angle scattering is at $150\ \mu\text{rad}$; hence, the transmission image spread would be $75\ \text{nm}$ and the ratio of the scattering was calculated to be $6.9\ \%$ of total by integrating Figure 23. From the aforementioned analysis it is clear that, a resolution of less than $100\ \text{nm}$ can be realized even in the experiment using UCNs by polishing both surfaces of the Si substrate.

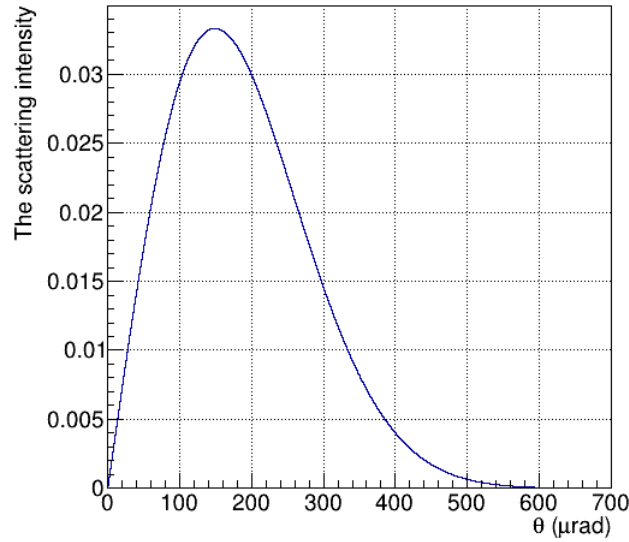


Figure 23. Scattering intensity with respect to scattering angle calculated by the micro-roughness model presented in [27] for a roughness amplitude $b = 0.60(4)\ \text{nm}$ and correlation length $w = 42(8)\ \mu\text{m}$

5 Conclusion

Different experiments use the system of a quantum bouncer, realized by the quantized states of cold neutrons or UCNs on a flat mirror in the Earth's gravitational field, to search for non-Newtonian interactions. For this purpose, neutron detectors with a high spatial resolution are used. In this study, we improved upon a detector so that it could measure the spatial distribution of UCNs with a high spatial resolution using a fine-grained nuclear emulsion. Two tasks were accomplished with the detector to conduct such measurements. The first task involved establishing a method to ensure that the high spatial accuracy and resolution can be achieved within a wide region of

65 mm \times 0.2 mm, for which reference marks were created using electron beam lithography. The second task involved the establishment of a method for the emulsion to work in vacuum, for which a holder was developed to maintain the volume around the emulsion at atmospheric pressure.

A transmission image of a Gd grating was acquired by cold neutron detection at BL05 of the J-PARC Material and Life Science Experimental Facility in Japan, and the resolution of the improved detector was evaluated by fitting the edge portion of the image with an error function. The results demonstrate that the intrinsic resolution of the detector was better than 0.56(8) μm for cold neutrons.

We successfully obtained the spatial distribution of quantized UCNs on a mirror using the improved detector at PF2 of the Institut Laue-Langevin in France. In addition, by comparing the distribution with the theoretical curve, it was found that the distribution was blurred by 6.9 μm , and it was understood that the main cause of the blurring was the effect of neutron refraction due to the large surface roughness on the upstream side (beam side) of the Si substrate. Thus, it has been shown that by polishing the upstream surface of the Si substrate, such a detector may be expected to obtain a resolution of less than 100 nm in experiments using UCNs.

Acknowledgments

We thank T. Naka for providing us fine-grained nuclear emulsion gel and advice regarding its use. We are grateful to T. Shinohara, T. Samoto, and A. Momose for his help in using the 9.00 μm Gd grating and its electron micrograph. We also thank P. Geltenbort for constructive advice and T. Brenner for his tremendous support on the experiment at Institut Laue-Langevin. The sputtering of the converter layer and test experiments for the development of the detector was conducted under the support of common use programs of the Institute for Integrated Radiation and Nuclear Science, Kyoto University. The reference marks were developed and created at Nagoya University Research Facility for Advanced Science and Technology with the assistance of T. Kato, D. Oshima and M. Sakashita. This research was supported by JSPS KAKENHI Grant Number 18H05210. The neutron experiment at the Materials and Life Science Experimental Facility of the J-PARC was performed under user programs (Proposal No. 2017B0336, 2018A0263, and 2019A0227) and S-type project of KEK (Proposal No. 2019S03).

References

- [1] Jiro Murata and Saki Tanaka. A review of short-range gravity experiments in the LHC era. *Classical and Quantum Gravity*, 32(3):033001, 2015.
- [2] Valery V Nesvizhevsky, H Börner, AM Gagarski, GA Petrov, AK Petukhov, H Abele, S Bäbler, Th Stöferle, and SM Soloviev. Search for quantum states of the neutron in a gravitational field: gravitational levels. *Nuclear Instruments and Methods in Physics Research Section A: Accelerators, Spectrometers, Detectors and Associated Equipment*, 440(3):754–759, 2000.
- [3] H Abele, T Jenke, D Stadler, and P Geltenbort. QuBounce: the dynamics of ultra-cold neutrons falling in the gravity potential of the Earth. *Nuclear Physics A*, 827(1-4):593c–595c, 2009.
- [4] G Ichikawa, S Komamiya, Y Kamiya, Y Minami, M Tani, P Geltenbort, K Yamamura, M Nagano, T Sanuki, S Kawasaki, et al. Observation of the spatial distribution of gravitationally bound quantum

- states of ultracold neutrons and its derivation using the Wigner function. *Physical Review Letters*, 112(7):071101, 2014.
- [5] Tobias Jenke, Gunther Cronenberg, Hanno Filter, Peter Geltenbort, Martin Klein, Thorsten Lauer, Kevin Mitsch, Heiko Saul, Dominik Seiler, David Stadler, Martin Thalhammer, and Hartmut Abele. Ultracold neutron detectors based on ^{10}B converters used in the qBounce experiments. *Nuclear Instruments and Methods in Physics Research Section A: Accelerators, Spectrometers, Detectors and Associated Equipment*, 732:1 – 8, 2013.
- [6] Cesare Mansueto Giulio Lattes, Giuseppe PS Occhialini, and Cecil Frank Powell. Observations on the tracks of slow mesons in photographic emulsions. *Nature*, 160(4067):486–492, 1947.
- [7] M Danysz, Krystyna Garbowska, Jacek Pniewski, T Pniewski, J Zakrzewski, ER Fletcher, Jacques Lemonne, Philippe Renard, Jean Sacton, WT Toner, et al. The identification of a double hyperfragment. *Nuclear Physics*, 49:121–132, 1963.
- [8] K Nakazawa et al. Double- λ hypernuclei via the ξ - hyperon capture at rest reaction in a hybrid emulsion. *Nuclear Physics A*, 835(1-4):207–214, 2010.
- [9] S Aoki, S Asai, SY Bahk, SH Chung, H Funahashi, CH Hahn, M Hanabata, T Hara, K Hoshino, M Ieiri, et al. Quasifree p (K^- , K^+) ξ - reaction in nuclear emulsion. *Nuclear Physics A*, 644(4):365–385, 1998.
- [10] K Kodama, N Ushida, C Andreopoulos, N Saoulidou, G Tzanakos, P Yager, B Baller, D Boehnlein, W Freeman, B Lundberg, et al. Final tau-neutrino results from the DONuT experiment. *Physical Review D*, 78(5):052002, 2008.
- [11] Takashi Asada, Tatsuhiro Naka, Ken-ichi Kuwabara, and Masahiro Yoshimoto. The development of a super-fine-grained nuclear emulsion. *Progress of Theoretical and Experimental Physics*, 2017(6):063H01, 2017.
- [12] N Naganawa, T Ariga, S Awano, M Hino, K Hirota, H Kawahara, M Kitaguchi, K Mishima, HM Shimizu, S Tada, et al. A cold/ultracold neutron detector using fine-grained nuclear emulsion with spatial resolution less than 100 nm. *The European Physical Journal C*, 78(11):1–7, 2018.
- [13] T Katsuragawa, A Umemoto, M Yoshimoto, T Naka, and T Asada. New readout system for submicron tracks with nuclear emulsion. *Journal of Instrumentation*, 12(04):T04002, 2017.
- [14] Tobias Jenke, Gunther Cronenberg, Hanno Filter, Peter Geltenbort, Martin Klein, Thorsten Lauer, Kevin Mitsch, Heiko Saul, Dominik Seiler, David Stadler, et al. Ultracold neutron detectors based on ^{10}B converters used in the qbounce experiments. *Nuclear Instruments and Methods in Physics Research Section A: Accelerators, Spectrometers, Detectors and Associated Equipment*, 732:1–8, 2013.
- [15] John Canny. A computational approach to edge detection. *IEEE Transactions on pattern analysis and machine intelligence*, (6):679–698, 1986.
- [16] Peter E Hart and RO Duda. Use of the Hough transformation to detect lines and curves in pictures. *Communications of the ACM*, 15(1):11–15, 1972.
- [17] Kenji Mishima, Takashi Ino, Kenji Sakai, Takenao Shinohara, Katsuya Hirota, Kazuaki Ikeda, Hiromi Sato, Yoshie Otake, Hitoshi Ohmori, Suguru Muto, et al. Design of neutron beamline for fundamental physics at J-PARC BL05. *Nuclear Instruments and Methods in Physics Research Section A: Accelerators, Spectrometers, Detectors and Associated Equipment*, 600(1):342–345, 2009.
- [18] Kenji Mishima. *Hamon Neutron Network News*, 25(156), 2015.

- [19] Yoshichika Seki, Takenao Shinohara, Wakana Ueno, Joseph D Parker, Tetsuo Samoto, Wataru Yashiro, and Atsushi Momose. Experimental evaluation of neutron absorption grating fabricated by oblique evaporation of gadolinium for phase imaging. *Physics Procedia*, 88:217–223, 2017.
- [20] Kanti V Mardia. Statistics of directional data. *Journal of the Royal Statistical Society: Series B (Methodological)*, 37(3):349–371, 1975.
- [21] Stefano Aghion, O Ahlén, C Amsler, A Ariga, T Ariga, AS Belov, Karl Berggren, G Bonomi, P Bräunig, J Bremer, et al. A moiré deflectometer for antimatter. *Nature communications*, 5(1):1–6, 2014.
- [22] R. L. Gibbs. The quantum bouncer. *American Journal of Physics*, 43(1):25–28, 1975.
- [23] Tobias Jenke, David Stadler, Hartmut Abele, and Peter Geltenbort. Q-BOUNCE—Experiments with quantum bouncing ultracold neutrons. *Nuclear Instruments and Methods in Physics Research Section A: Accelerators, Spectrometers, Detectors and Associated Equipment*, 611(2-3):318–321, 2009.
- [24] L. A. Chizhova, S. Rotter, T. Jenke, G. Cronenberg, P. Geltenbort, G. Wautischer, H. Filter, H. Abele, and J. Burgdörfer. Vectorial velocity filter for ultracold neutrons based on a surface-disordered mirror system. *Physical Review E*, 89(3):032907, 2014.
- [25] VV Nesvizhevsky, A Yu Voronin, P-P Crépin, and S Reynaud. Interference of several gravitational quantum states of antihydrogen in GBAR experiment. *Hyperfine Interactions*, 240(1):1–9, 2019.
- [26] S.K. Sinha, E.B. Sirota, S. Garoff, and H.B. Stanley. X-ray and neutron scattering from rough surfaces. *Physical Review B*, 38(4):2297, 1988.
- [27] A Steyerl. Effect of surface roughness on the total reflexion and transmission of slow neutrons. *Zeitschrift für Physik A Hadrons and nuclei*, 254(2):169–188, 1972.